Physics in Medicine & Biology

High resolution monolithic LYSO detector with 6-layer depth-of-interaction for clinical PET

To cite this article before publication: Mariele Stockhoff *et al* 2021 *Phys. Med. Biol.* in press https://doi.org/10.1088/1361-6560/ac1459

IOP Publishing Journal Title
Journal **XX** (XXXX) XXXXXX https://doi.org/XXXX/XXXX

High resolution monolithic LYSO detector with 6-layer Depth-Of-Interaction for clinical PET

Mariele Stockhoff[1], Milan Decuyper[1], Roel Van Holen[1] and Stefaan Vandenberghe[1]

[1] Department of Electronics and Information Systems, Medical Image and Signal Processing (MEDISIP), Ghent University, Ghent, Belgium

E-mail: mariele.stockhoff@ugent.be

Received xxxxxx
Accepted for publication xxxxxx
Published xxxxxx

Abstract

The system spatial resolution of whole-body positron emission tomography (PET) is limited to around 2 mm due to positron physics and the large diameter of the bore. To stay below this 'physics'-limit a scintillation detector with an intrinsic spatial resolution of around 1.3 mm is needed. Currently used detector technology consists of arrays of 2.6-5 mm segmented scintillator pixels which are the dominant factor contributing to the system resolution. Pixelated detectors using smaller pixels exist but face major drawbacks in sensitivity, timing, energy resolution and cost.
Monolithic continuous detectors, where the spatial resolution is determined by the shape of the light distribution on the photo detector array, are a promising alternative. Without having the drawbacks of pixelated detectors, monolithic ones can also provide depth-of-interaction (DOI) information.
In this work we present a monolithic detector design aiming to serve high-resolution clinical PET systems while maintaining high sensitivity. A 50 x 50 x 16 mm^3 Lutetium- Yttrium oxyorthosilicate (LYSO) scintillation crystal with silicon photomultiplier (SiPM) back side readout is calibrated in singles mode by a collimated beam obtaining a reference dataset for the event positioning. A mean nearest neighbour (MNN) algorithm and an artificial neural network for positioning are compared.
The targeted intrinsic detector resolution of 1.3 mm needed to reach a 2 mm resolution on system level was accomplished with both algorithms. The neural network achieved a mean spatial resolution of 1.14 mm FWHM for the whole detector and 1.02 mm in the centre (30 x 30 mm^2). The MNN algorithm performed slightly worse with 1.17 mm for the whole detector and 1.13 mm in the centre. The intrinsic DOI information will also result in uniform system spatial resolution over the full field of view.

Keywords: monolithic detector, high-resolution, PET, TB-PET

1. Introduction

Spatial resolution of positron emission tomography (PET) systems is limited by the intrinsic detector resolution, the system diameter and the positron range of the tracer isotope. Almost all recent clinical PET scanners are based on detectors with pixelated Lutetium- Yttrium oxyorthosilicate (LYSO) crystal arrays coupled to silicon photomultipliers (SiPMs) (Siemens Biograph Vision^{TM} (van Sluis *et al* 2019), GE Discovery^{TM} MI (Pan *et al* 2019), Philips Vereos (Rausch *et al* 2019) and United Imaging uMI 780 (Spencer *et al* 2020)(Hu *et al* 2021)). The intrinsic detector spatial resolution of those detectors is limited by their crystal pixel widths ranging from 2.6 mm to 5 mm. For a system with a diameter of 60-80 cm the introduced noncollinearity limits the achievable spatial resolution to around 2 mm. Therefore, the ideal detector resolution R_{int} should be better than 1.3 mm to not have a significant effect on the system spatial resolution limit. This is calculated from the system resolution definition $R_{sys} \approx \sqrt{R_{det}^2 + R_{range}^2 + R_{180^\circ}^2}$, where for monoliths $R_{det} \approx \frac{R_{int}}{\sqrt{2}}$, the positron range of ^{18}F is $R_{range} = 0.2\ mm$ and the noncollinearity dependent on the system diameter D is $R_{180^\circ} = 0.0022\ \times\ D$ (Cherry et al 2012)(Vandenberghe et al 2020) (Levin and Hoffman 2000). A conventional pixelated detector can also reach the spatial resolution of 1.3 mm and better, but at the same time the costs are increasing because the detector then consists of more and thinner crystals which impede the manufacturing procedure. A decreasing pixel size also leads to a reduced light collection and a deterioration of timing performance (Berg and Cherry 2018). Nevertheless, the current state-of-the-art coincidence timing resolution (CTR) is 214 ps FWHM based on pixelated arrays of 3.2 x 3.2 x 20 mm^3 (van Sluis *et al* 2019). For monoliths the light spread and collection over multiple photodetector pixels results in low SNR and thus limits the achievable timing performance (Lamprou *et al* 2020, Borghi *et al* 2016b). However, the unrestricted movement of scintillation photons with a direct travel path to the photodetector makes monolithic crystals fundamentally superior to be used for timing measurements. We believe that the monolith is a promising alternative to reach timing performances comparable or better than those of pixelated detectors using precise calibration techniques and/or simulated data to train neural networks.

Furthermore, the longer the axial field of view, the more oblique gamma rays will interact with the crystal, leading to parallax errors and decrease in spatial resolution when no depth-of-interaction (DOI) measurement is present. DOI determination is a unique feature of monolithic crystals that cannot easily be extracted from pixelated crystals (Ito *et al* 2011). Long axial field-of-view (FOV) PET devices, also called total-body (TB) - PET scanners (Vandenberghe *et al* 2020, Surti *et al* 2020), have recently been prototyped (Spencer *et al* 2020, Karp *et al* 2020) and thereafter emerged on the imaging market (United Imaging uExplorer, Siemens Biograph Vision Quadra). These scanners can have an axial length of up to 2 m leading to great sensitivity increase and the possibility to measure dynamic processes in the entire human body simultaneously. However, this axial extension requires many more gamma-ray detectors constituting an enormous cost factor. The PET20.0 consortium was formed aiming to build a cost-efficient more compact TB-PET scanner with a system spatial resolution of 2 mm (Vandenberghe *et al* 2017). The only currently existing TB-PET systems employ pixelated detectors of 2.76 mm and 3.76 mm crystal width leading to system resolutions of 3.0 mm (Spencer *et al* 2020) and 4.0 mm (Karp *et al* 2020) respectively. These systems do not have DOI capabilities. At off-centre positions the spatial resolution therefore degrades to 4.7 mm and 5.6 mm FWHM. More recently the Biograph Vision Quadra system with long axial FOV was presented with pixel width of 3.2 mm (Alberts *et al* 2021).

The aim of this work is to develop a gamma-ray detector that can provide good spatial resolution and sensitivity while being cost-efficient. Monolithic detectors are an alternative detector design consisting of a continuous scintillation crystal coupled to an array of SiPMs. The scintillation light spreads inside the crystal and the light distribution can be sampled by the SiPM array. From the shape of this distribution the 3D interaction position i.e., the 2D position and DOI can be accurately determined. As mentioned above, for TB-PET scanners DOI becomes more important as there is also parallax effects and degradation in the axial direction (axial blurring). At the same time, DOI improves spatial resolution for larger radial distances in dedicated organ scanners where the small bore induces oblique incidence angles. It minimizes parallax effects and therefore provides a more uniform resolution across the bore and allows smaller system diameters (Thoen *et al* 2013). Furthermore, DOI is of interest for TOF - PET to correct for the time walk inside the detector (Lecoq *et al* 2020). Another advantage of monoliths compared to pixelated detectors is that there is no sensitivity loss due to dead space. The higher the resolution requirements for a pixelated detector the more dead spaces are created between the pixels and the larger the sensitivity loss. For a 1 mm pixelated array a scintillation material loss of 14% was calculated compared to the monolithic detector, adding up to 26% loss in coincidence (Stockhoff *et al* 2019).

Monolithic detectors provide high spatial, timing, energy resolution, and sensitivity, while the single detector is significantly cheaper compared to a pixelated crystal with the same resolution (Borghi *et al* 2016b, Marcinkowski *et al* 2016, Gonzalez-Montoro *et al* 2021). The unit cost for e.g. a 1 mm pixelated array stated by two manufacturers is 1.5-1.75 higher than for a monolithic crystal of the same size (Stockhoff *et al* 2019). A 1-1.5 m long PET system can consist of 800-1200 detectors. According to (Vandenberghe *et al* 2020) crystal cost can constitute up to 46-48% of the total cost of a long axial FOV PET scanner. One should also keep in mind that if all photodetector channels are read out, the count rate performance of the electronics needs to be much higher for monolithic detectors compared to pixelated ones. Various techniques to reduce the number of readout channels have been evaluated e.g., Anger logic, row and column summing or a sparse readout (González-Montoro *et al* 2018, Chinn *et al* 2013, Pierce *et al* 2014, Yang *et al* 2019). However, these techniques should be implemented cautiously since performance parameters like spatial resolution can degrade but especially timing resolution is sensitive to multiplexing (Lamprou *et al* 2020, Gundacker *et al* 2016).

There are some other drawbacks related to monolithic detectors. First of all, there is the more complex positioning, which has only recently become possible in real time due to more advanced hardware like GPUs. Secondly, there is the more elaborate calibration procedure to acquire reference data for the positioning algorithms being used. Often reference signals are acquired by a tiny calibration beam in a narrow 2D grid over the whole detector. Techniques to speed up the calibration already exist (Freire *et al* 2019, España *et al* 2013, Miyaoka *et al* 2010, Müller *et al* 2018).

Most commonly used positioning algorithms are statistical ones, such as maximum likelihood estimation (Pierce *et al* 2018, Ling *et al* 2007, España *et al* 2014), k- nearest neighbour (van Dam *et al* 2011, Borghi *et al* 2016a), and more recently other machine learning algorithms like gradient tree boosting (Müller *et al* 2018) and neural networks (Wang *et al* 2013, Bruyndonckx *et al* 2004, Iborra *et al* 2019, Decuyper *et al* 2021). Multiple detector designs have been evaluated with respect to spatial resolution. The performance depends highly on the crystal thickness. For the use in clinical systems a thickness of more than 12 mm is typically required to have sufficient detector sensitivity. A spatial resolution of 1.7 and 1.5 mm FWHM could be achieved with a 22 and 20 mm thick crystal, respectively (Borghi *et al* 2016a, 2015). A 15 mm thick crystal was used in (González-Montoro *et al* 2018) achieving 1.8 mm FWHM. In (Müller *et al* 2018) a spatial resolution of 1.4 mm (with correction of source size) could be obtained with a crystal thickness of 12 mm. Even better spatial resolution of 1.1 mm (Borghi *et al* 2015) and 0.78 mm (Mollet *et al* 2017) could be achieved with a 10 and 8 mm thick crystal. Not only the crystal thickness but also the evaluated region on the detector (centre, edge, corner, centre line on one axis) and the correction methods applied to isolate the calibration beam diameter (González-Montoro *et al* 2019) have a large impact on the stated spatial resolution. There is no standardized procedure to evaluate the performance of monolithic detectors and therefore it is not trivial to compare results from different groups.

In this document we present a high-resolution monolithic detector design aiming to serve the TB-PET system in the PET20.0 project, but also a potential candidate for other brain or clinical PET systems with similar requirements. A 50 x 50 x 16 mm^3 LYSO scintillation crystal with backside SiPM readout is calibrated in singles mode by traversing a collimated beam in a 2D grid to obtain a dataset of events that serve as references for the event positioning. Two positioning algorithms are compared, a mean nearest neighbour algorithm (MNN) (Stockhoff *et al* 2019) and an artificial neural network (Decuyper *et al* 2021). The MNN algorithm is well-studied and implemented in commercial PET systems while neural network development is still evolving and promising for high-performance positioning. We study with extensive measurements the intrinsic spatial resolution and DOI performance of this detector for both positioning algorithms.

2. Materials and Methods

2.1 Experimental setup

The investigated detector is a monolithic 50 x 50 x 16 mm^3 LYSO (Epic Crystal) crystal, readout by silicon photomultipliers (SiPMs) at back (Figure 1 a), b)). The surfaces have a rough black painted finishing on the crystal sides (16 x 50 mm^2) and a black-painted specular reflector attached to a polished crystal top (50 x 50 mm^2). The crystal is coupled with optical grease (St. Gobain BC630) to an 8 x 8 array of 6 x 6 mm^2 SiPMs (ON Semiconductor® MicroFJ-60035-TSV). The crystal and SiPMs are placed in a light-tight aluminium housing. Similar to what has been previously published (Deprez *et al* 2011, Mollet *et al* 2017, Krishnamoorthy *et al* 2018) the signals of 64 SiPM pixels are combined to 16 (8+8) channels by summing rows and columns (Figure 2). This is done by using a resistor network that splits the current of each pixel in two. One half of the current ends up in the column signal and the other half ends up in the row signal. The 16 rows and columns currents are then amplified using a current-to-voltage amplifier (based on an operational amplifier). In a next step the amplified signal is converted to a differential signal, using a differential amplifier. The differential signal is digitized by a free-running ADC with a sampling frequency of 64 MHz.

2.2 Calibration data acquisition

The detector is calibrated with a collimated ^{68}Ge source (69 MBq) placed in a tungsten collimator forming a beam with a diameter of 0.6 mm and 1 mm respectively. The beam is first collimated to 1 mm for 48 mm and then further collimated to 0.6 mm (1 mm) for 12 mm respectively (Figure 1 d)). The collimated beam is orthogonal to the optical table irradiating the detector which is mounted on a three-dimensional robot stage (Owis LTM 80, positioning error 25 µm/100 mm) (Figure 1 a)). Calibration data is acquired in a 49x49 grid for 70s per position. A calibration and an evaluation dataset are extracted from the acquired data. For the calibration dataset the events are pre-positioned with an Anger logic algorithm for each calibration position. A region of interest (ROI) is then drawn around the calibration beam position to extract only data from the irradiated position and to avoid events from the intrinsic ^{176}Lu radiation of the scintillator. An energy window of 20% is applied. For the neural network validation an additional dataset is acquired at 1 mm grid steps in the detector centre (10 x 10) with an offset of 0.5 mm with respect to the calibration positions. This validation set is acquired to avoid overfitting (more detail in section 2.4). For clarity we summarize that for both algorithms the training (calibration) data is energy filtered and a position filter is applied. For the evaluation (test) dataset an energy filter but no ROI selection (no position filter) is applied. Therefore, only those scattered events are filtered that have not deposited their full energy in the detector (i.e., Compton interaction then gamma exits the crystal).

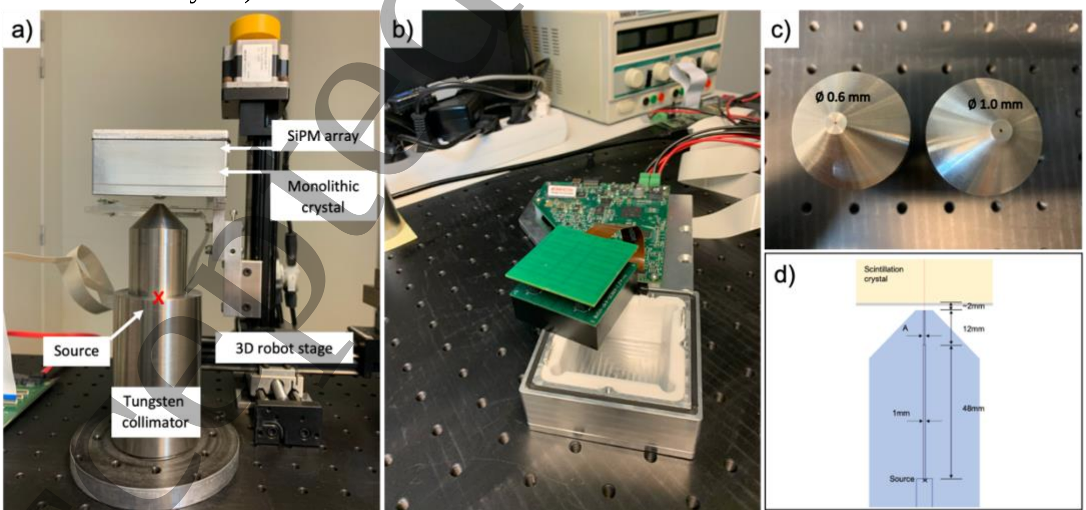

Figure 1 a) The calibration setup consists of a collimator forming the calibration beam and the detector that is mounted on a 3D robot stage. b) The light-tight aluminium housing encapsulates the black-painted scintillation crystal coupled to the SiPM array. c) The collimators have holes of 0.6 mm and 1 mm diameter. d) Sketch of the collimator geometry. Diameter A represents 0.6 mm or 1 mm, respectively.

2.3 Mean Nearest Neighbour (MNN) positioning algorithm

The calibration data for the MNN algorithm is extracted from the Anger histogram as a ROI of in total 37 high intensity pixels (pixel size = 0.26 mm). The remaining number of events per position for the 0.6 mm beam is on average 4930 ± 730 and for the 1.0 mm beam 9796 ± 1577. Each event first undergoes a baseline correction and is normalized by dividing the signal in each channel by the sum of all 16 channels to make it energy independent. For each single event we calculate the variance between the values of the 16 channel signals. These variances are then used to sort the calibration events into 6 groups. For example, the first group includes signals with small variances referring to events that interacted at the top of the crystal where the light spread is broad and many SiPM pixels have a similar value. On the contrary, the sixth group includes events where the gamma interaction occurred close to the SiPM array and most of the light is captured by a small number of SiPM pixels and therefore the signal has a larger variance. The final step is to calculate the mean signal in each of the channels per group. For each calibration position we then end up with 6 reference signals which are the mean of all the events per "depth"-group. In Figure 2 c) these mean signals are presented for a calibration position in the detector centre. The number of events per group, here called layers, best resembles the expected depth distribution derived from Beer-Lambert attenuation Law with these splits: 29.5%, 22.95%, 17.87%, 13.91%, 10.83% and 4.94% for layer 1 to 6 respectively (Figure 6). For simplicity we assume the beam to be perpendicular, however, a certain opening angle is introduced by the collimator geometry (Figure 1 d)).

The six layers do not only provide depth information but also improve 2D spatial resolution (Ling *et al* 2007). The reason for the improvement is that the signal at one 2D position varies greatly between the different interaction depths. Using a single mean signal over all interaction depths would be a too general representation of the signal variety. Therefore, using mean events from different (here six) depth-groups lead to a better position determination using the mean nearest neighbour algorithm. The ideal number of layers is determined in section 2.5.6. For each layer the mean signal is calculated, interpolated to a grid size 0.26 mm and stored in look-up-tables. The evaluation data is positioned with a nearest neighbour algorithm implemented in Matlab ('knnsearch'-function). In an exhaustive neighbour search, each test event is compared to all reference signals from all six depth layers. The calibration signal with the calculated least distance to the test signal is the selected nearest neighbour. More details can be found in (Stockhoff *et al* 2019).

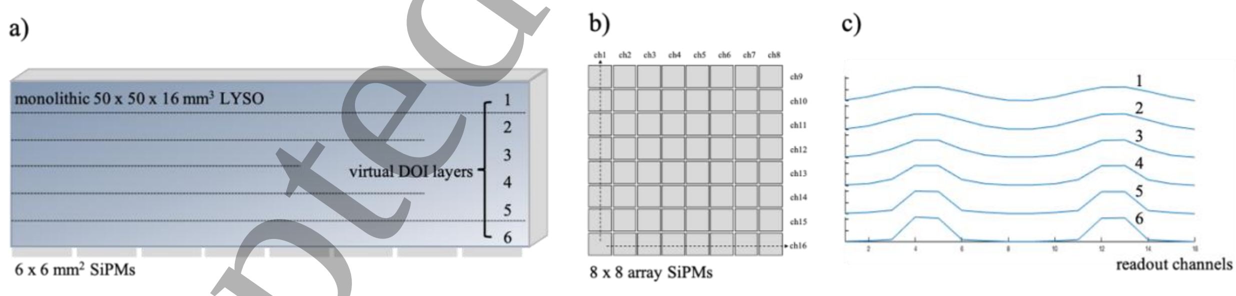

Figure 2 a) Detector geometry with SiPM readout and virtual DOI layers. b) The signals of the 64 SiPM pixels are summed per row and column to a total of 16 readout channels. c) 16-channel mean signal per depth-group for a calibration position in the detector centre. The channel variance is smaller in layer 1 and increases towards layer 6.

2.4 Neural network positioning algorithm

The calibration data for the neural network is defined by a ROI of 109 high intensity pixels (pixel size = 0.26 mm) in the Anger histogram. The ROI is larger for the neural network calibration dataset than in the MNN dataset. A larger ROI includes more scattered events and especially the ones that scattered with a larger angle in a direction more parallel to the entrance face. While the neural network training profits from the 'far'- scattered events and learns to position them, the MNN algorithm filters scattered events in the process of taking the mean signal of many events. Therefore, it is counterproductive to include more scattered events in the MNN training dataset. A fully connected artificial neural network is designed with 16 inputs (from 8+8 SiPM signals), three hidden layers containing each 256 neurons and three outputs (x, y and z position coordinates) as illustrated in Figure 3. Leaky ReLU activation is added after every hidden layer. The network is trained using the AdamW optimization algorithm with an initial learning rate of 10^{-3}, a mini-batch size of 256 events and L1 loss between predicted and ground truth calibration position as optimization metric. L2 weight decay is set to 10^{-2}. The calibration beam positions were used as ground truth x and y coordinates. The z coordinate label was set to the DOI layer (label 1 to 6) the event belongs to as obtained from the events' variance (similar to section 2.3). The number of events per calibration position is split with 28.85% for layer 1 with the smaller variances, 22.03% for layer 2, 17.4% layer 3, 13.8% layer 4, 10.85% layer 5 and 8.07% for layer 6 with the larger variances. Each event is independently standardized to zero mean and unit variance. The training set contains 1000 events per calibration position and one training epoch is defined as an iteration over 100 events per position randomly extracted from the training set. After every epoch, the network is validated on data acquired in a 1 mm intermediate grid in the detector centre (9x9 mm^2, 10x10 positions, 1000 events/position). This allows to regularly check and prevent potential overfitting on the training grid positions. Based on the validation loss, learning rate is halved every 10 epochs without improvement and training is stopped if the loss did not improve for 50 epochs. The deep learning methodology is implemented in python using PyTorch and the network is trained on an 11 GB NVIDIA RTX 2080Ti GPU. Optimization of the network architecture, training set size and training procedure was done based on simulation data of the same setup. For full detail we refer the reader to (Decuyper *et al* 2021).

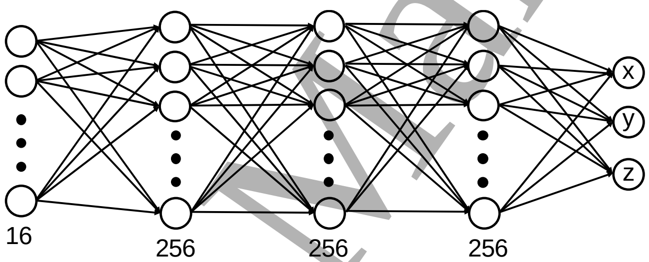

Figure 3 Neural network architecture. Input of 16 (8+8 summed row and column) signals and three output coordinates x, y and z.

2.5 Performance evaluation

The performance is evaluated based on two parameters: FWHM and 1D/2D-bias. The FWHM [mm] is the full width at half maximum of the Gaussian fit to the horizontal and vertical line profile of the point spread function (PSF) in the 2D histogram of all events from all depths per calibration position. For the estimation of the FWHM we need the peak value of the distribution and the width of the distribution at half the peak value. To determine these two parameters most accurately, we fitted a Gaussian to the central peak region (including all values over a threshold T = 0.25 * peak value). The FWHM could also be evaluated simply by extracting the peak of the distribution and the width of the distribution at half the maximum without fitting a function to the distribution. The low sampling on the x-axis, however, does not allow to determine the FWHM at exactly the half maximum. Therefore, an interpolation between the data points or a fit is needed to determine these values. The positioning bias [mm] is the distance between the peak of the PSF and the known calibration position in x and y direction. The 2D bias [mm] is the 2D distance between the peak of the PSF and the true calibration position. Mean and median values are evaluated for the full detector (5x5 cm^2) and the detector centre (3x3 cm^2), respectively. Note that PSFs at the detector edges mostly do not resemble a Gaussian distribution resulting in inaccurate FWHM values. As an alternative measure for spatial resolution over the whole detector including the edges the bar phantom measurement can be used.

2.5.1 Spatial resolution estimation with a 0.6 mm and 1.0 mm calibration beam

The collimated calibration beam should ideally deliver an infinitely small beam diameter that generates gamma interactions at ground-truth positions. However, the collimator is limited to a certain diameter by (i) the manufacturing feasibility and (ii) the limited statistics with small beams. We test two calibration beams with diameter 0.6 mm and 1.0 mm respectively to evaluate their effect on the achievable spatial resolution with the two positioning algorithms. Two sets of calibration data are obtained, using a calibration beam collimated to 0.6 mm and 1 mm beam respectively. The two MNN reference datasets and two trained neural networks are then tested with the evaluation dataset from the smaller collimated beam. This is done because the smaller beam can provide data that is closer to the ground truth position. The evaluation dataset includes 30000 energy-filtered events (20% energy window) per position without ROI selection. The results are not corrected for the remaining source size of 0.6 mm. A bias correction for the 2D - position between the two calibrations is done with 0.3 mm and 0.18 mm in x-direction and 0 mm and -0.18 mm in y-direction for the MNN algorithm and neural network positioning respectively. The bias originates from the disassembly and assembly steps in between the two calibrations.

2.5.2 DOI estimation

For positioning with the MNN algorithm each of the reference events automatically belongs to a certain depth-layer defined by the signal variance and therefore DOI of the event. The principle is described in detail in section 2.3. For the neural network the DOI is determined by a network trained on the DOI labels defined by the signal variance. This is explained in section 2.4.

To evaluate the DOI estimation of both algorithms the predicted relative number of events in each of those layers is compared. We compare to (i) the theoretical number of events that we expect by the attenuation of the crystal according to Beer-Lambert Law and (ii) the results we previously obtained from optical simulations (Stockhoff *et al* 2019) modelling the same detector geometry, calibration procedure and MNN positioning. Note that in the simulations the DOI was evaluated for only the centre 10 x 10 mm^2. Here, we use the calibration dataset from the 1.0 mm beam with 109 pixels (2.5.1).

2.5.3 Energy resolution

The energy resolution is evaluated per calibration position. The sum of each event signal from the calibration dataset (1.0 mm beam, 37 pixels) is histogrammed and a Gaussian is fit to the distribution. Similar to what is described in section 2.5. the Gaussian is fitted to the photopeak so that the fit accurately represents the peak of the actual distribution and the width at half maximum. To determine these two parameters most accurately, we fitted a Gaussian to the central peak region (including all values over a threshold T = 0.25 * peak value). Figure 7 shows the original distribution and the Gaussian fit. A remainder of the background signal (^{176}Lu) is present in the energy histograms and explains the counts higher than what is expected from the Germanium source. The fit does not consider the tails from the Lutetium contamination.

2.5.4 Uniformity

A ^{68}Ge source (29 MBq) is placed at a distance of 52.5 cm of the detector. The acquired events are filtered with an energy window of 20% and then positioned with the MNN algorithm and neural network. The uniformity is further analysed by selecting the positioned events per DOI layer.

2.5.5 Bar phantom

Additional to the analysis of the point spread function, a four-quadrant bar phantom designed for this study gives a more visual impression on the detector performance. With this phantom the spatial resolution of the detector can be assessed by its capability to resolve adjacent bars. Furthermore, spatial linearity can be visually inspected. The phantom is a 60 x 60 x 15 mm^3 tungsten block in which slits of 0.6, 0.8, 1.0 and 1.2 mm are machined by wire erosion (Figure 4). The phantom is placed directly on the detector while the ^{68}Ge source (29 MBq) is placed at 52.5 cm distance. For each of the four phantom quadrants a separate measurement is done by positioning the source in the respective quadrant centre as seen in Figure 4. This way the entrance angles are more perpendicular and less gamma rays penetrate the thin bars worsening the contrast of the test pattern. Recorded events are filtered with an energy window of 20% and positioned with the MNN algorithm and the neural network. The flood source histograms from section 2.5.4. are used to normalize for uniformity. The line profiles are not taken at one discrete position but are summed for each respective quadrant in the direction parallel to the bar pattern. The minima O_{min} and maxima O_{max} are determined in the summed line profile (Figure 11, between 0 and 60) to calculate the output modulation $M_{out} = \frac{O_{max}-O_{min}}{O_{max}+O_{min}}$. The input modulation $M_{in} = \frac{I_{max}-I_{min}}{I_{max}+I_{min}}$ is obtained from Gate simulations. The STL file of the bar phantom is loaded into the simulation software. The detector is modelled in Gate with the same geometry, SiPM pixel size and surface finish as in the presented prototype. More details on simulation parameters can be found in (Stockhoff *et al* 2019). The positions of the gamma rays absorbed in the crystal are recorded for the four measurement scenarios (source positions x_1 to x_4 in Figure 4 b)). Similar to the experimental analysis the line profiles are then summed for each respective quadrant in the direction parallel to the bar pattern. Then the input modulation M_{in} for all four bar widths is calculated. The simulated M_{in} value is almost constant over the detector but does not include events from lutetium background. Due to that and since a simulation represents an idealized environment a rather high input modulation value between 0.93 and 0.95 is calculated. For the determination of the MTF it means that the results shown here are rather on the pessimistic side and might be better in reality. Finally, the modulation transfer function (MTF) is calculated for each bar width w $MTF(w) = M_{out}(w)/M_{in}(w)$.

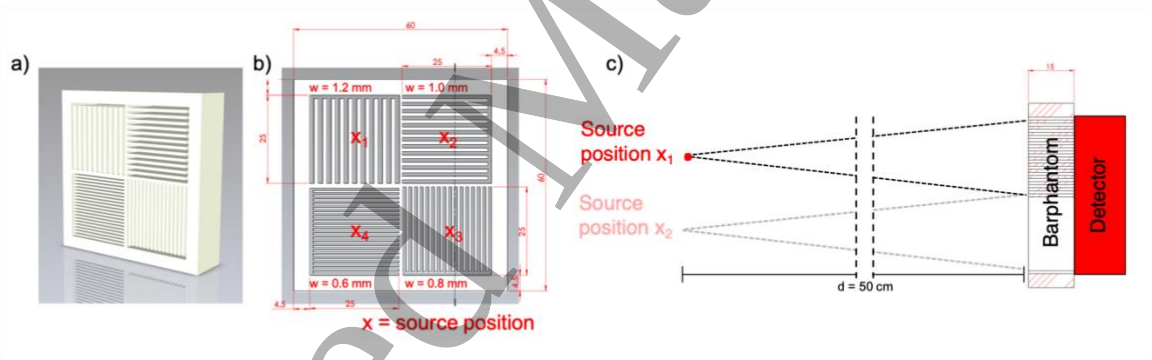

Figure 4 a) 3D view of the four-quadrant bar phantom. b) Dimensions of bar phantom and source positions x_1-x_4. c) Side view of the experimental setup.

2.5.6 2D resolution improvement by adding DOI layers

For the MNN positioning algorithm the calibration data per position is divided into groups according to the signal's variance. For each group the mean signal is calculated and stored as a reference signal. Since the variance is related to the DOI of the signal we call these groups DOI layers or simply layers. Here the effect of the number of chosen DOI layers on the 2D resolution is evaluated. The acquired events from the bar phantom measurements in 2.5.4 are positioned with reference datasets calculated with different number of layers. For 1, 2, 4, 6, 8, and 10 layers the 2D resolution is compared visually. A quantitative comparison is provided by MTF values (Figure 12) that are determined the same way as in 2.5.5.

3. Results

3.1 Spatial resolution estimation with a 0.6 mm and 1.0 mm calibration beam

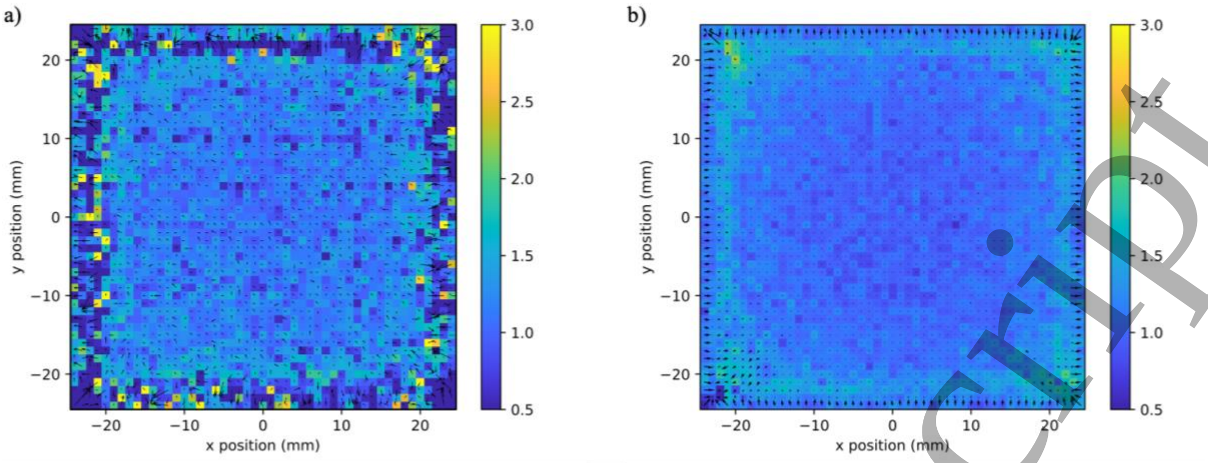

Figure 5 Spatial resolution as FWHM [mm] for detector with 0.6 mm diameter calibration beam. The bias vectors are indicated as arrows for a) MNN event positioning and b) Neural network positioning.

The spatial resolution obtained for the detector calibrated with the 0.6 mm beam is shown in Figure 5 for the MNN algorithm and the neural network respectively. For the MNN algorithm a FWHM of 1.17 mm is obtained (Table 1). The mean x and y bias is 0.37 mm and the resulting 2D bias is 0.59 mm. For the neural network mean and median FWHM is obtained of 1.14 mm and 1.10 mm. The mean x,y bias is 0.13/0.11 mm and the resulting 2D bias is 0.20 mm. A general degradation is seen towards the edges of the detector. In the detector centre 30 x 30 mm^2 the mean FWHM value is 1.13 mm for MNN and 1.02 mm for the neural network.

Table 1 Performance parameters for calibration of detector with 0.6 mm diameter calibration beam.

	MNN		*Neural network*	
	50 x 50 mm^2	*30 x 30 mm^2 centre*	*50 x 50 mm^2*	*30 x 30 mm^2 centre*
FWHM mean	1.17	1.13	1.14	1.02
FWHM median	1.17	1.14	1.10	1.01
Bias x mean	0.37	0.14	0.13	0.06
Bias y mean	0.37	0.16	0.11	0.05
Eucl. distance/ 2D Bias	0.59	0.26	0.20	0.09

A calibration with a 1 mm diameter collimator leads to a mean and median FWHM of 1.23 mm and 1.21 mm when positioning 0.6 mm beam data with MNN (Table 2). The neural network can keep up the overall mean resolution of 1.5 mm FWHM and median of 1.0 mm. Therefore, the larger collimator diameter only slightly degrades the mean and median FWHM values for MNN while with the neural network the values are stable. The bias decreased slightly for MNN and for the neural network.

Table 2 Performance parameters for calibration of detector with 1.0 mm diameter calibration beam.

	MNN		*Neural network*	
	50 x 50 mm^2	*30 x 30 mm^2 center*	*50 x 50 mm^2*	*30 x 30 mm^2 center*
FWHM mean	1.23	1.16	1.15	1.02
FWHM median	1.21	1.16	1.10	1.02
Bias x mean	0.29	0.13	0.12	0.05
Bias y mean	0.26	0.10	0.12	0.05
Eucl. Distance/ 2D bias	0.46	0.20	0.19	0.09

3.2 DOI estimation

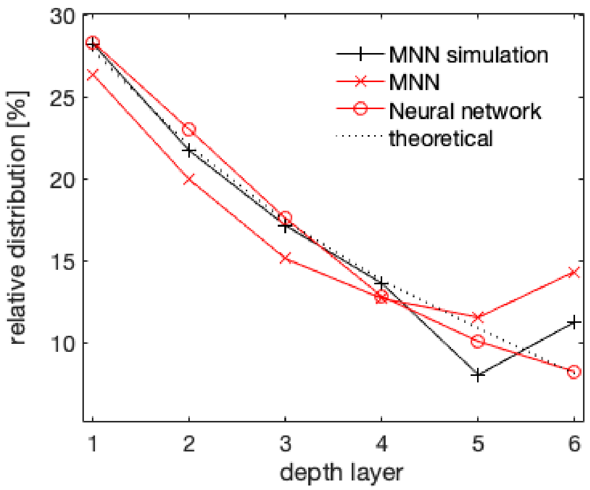

Figure 6 DOI evaluation. The distribution of events positioned in each layer.

In Figure 6 the relative distribution of the identified DOI layer is presented in red for the two algorithms presented in this paper. As a reference the theoretical distribution that we expect by the attenuation of the crystal is shown as a dotted black line. The results obtained from simulations (Stockhoff *et al* 2019) with the MNN algorithm is shown as a black solid line.

For the MNN algorithm an offset of 1-2% can be observed in layer one to four compared to the theoretical curve. The sixth layer contains about 6% more events than expected. The depth distribution obtained from simulations with the same algorithm also shows a significant higher amount of events positioned in layer 6 than expected from the theoretical distribution. This has been investigated and is explained in the discussion. The neural network fits the theoretical curve with a maximum offset of 0.8%.

3.3 Energy resolution

The evaluation of the energy resolution per calibration position is shown in Figure 7. The energy resolution for the whole detector is 11.03% ± 1.1% and 10.7% ± 0.5% for the detector centre (30 x 30 mm^2). Degradations of up to 18% can be observed in the top left and right corner regions at 6-7 mm from the crystal edge. The bottom corner region degrades to 14-15%. The energy spectrum includes small amounts of ^{176}Lu background radiation from the LYSO scintillator which explain the counts above 511 keV in Figure 7 a) (Alva-Sánchez *et al* 2018).

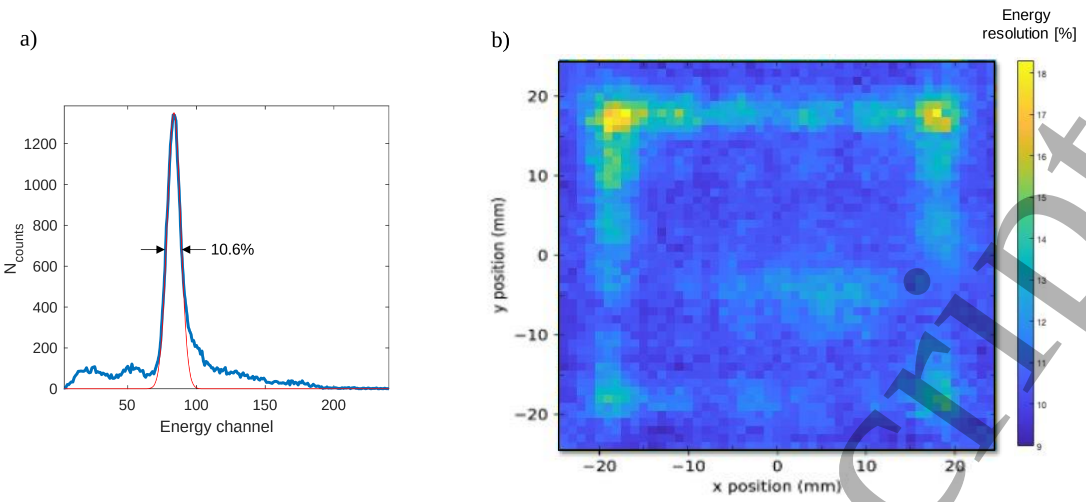

Figure 7 a) The energy spectrum at a calibration position in the detector centre with Gaussian fit and energy resolution of 10.6% FWHM. b) The mean energy resolution of the detector per calibration position is 11.03%.

3.4 Uniformity

In Figure 8 the detector uniformity is shown for the MNN positioning algorithm and the neural network. Both histograms show artifacts related to the underlying 8x8 SiPM pixel array. Furthermore, the MNN histogram shows bright hotspots while the neural network histogram shows more wrinkle-like artifacts.

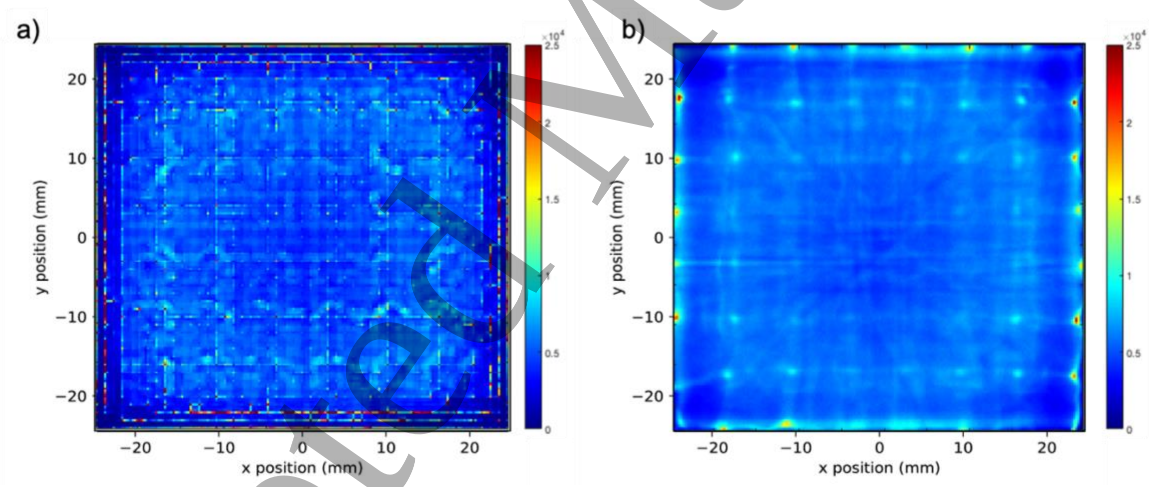

Figure 8 Detector uniformity. 2D histogram of positioned events from a flood source using a) the MNN positioning algorithm and b) the neural network positioning.

A better understanding of the non-uniformities can be obtained by looking at the 2D histograms per DOI layer in Figure 9. From left to right, the uniformity can be observed from the crystal top (gamma entrance face) to the readout (SiPM array) side of the detector. Especially in layer 6 the uniformity suffers from the underlying SiPM structure.

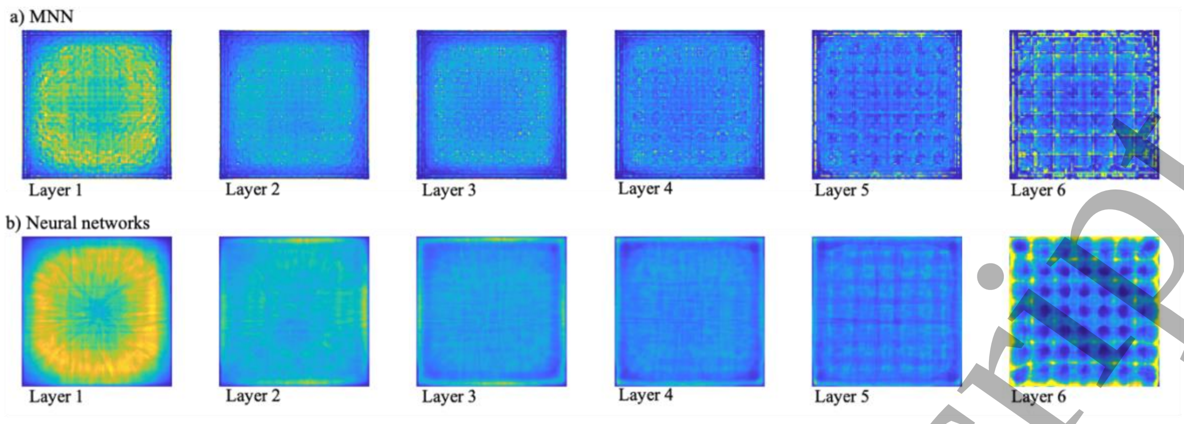

Figure 9 The detector uniformity presented per DOI layer. Layer 1 is the gamma entrance face and layer 6 is close to the SiPM array. 2D histograms for a) the MNN positioning and b) the neural network positioning.

3.5 Bar phantom

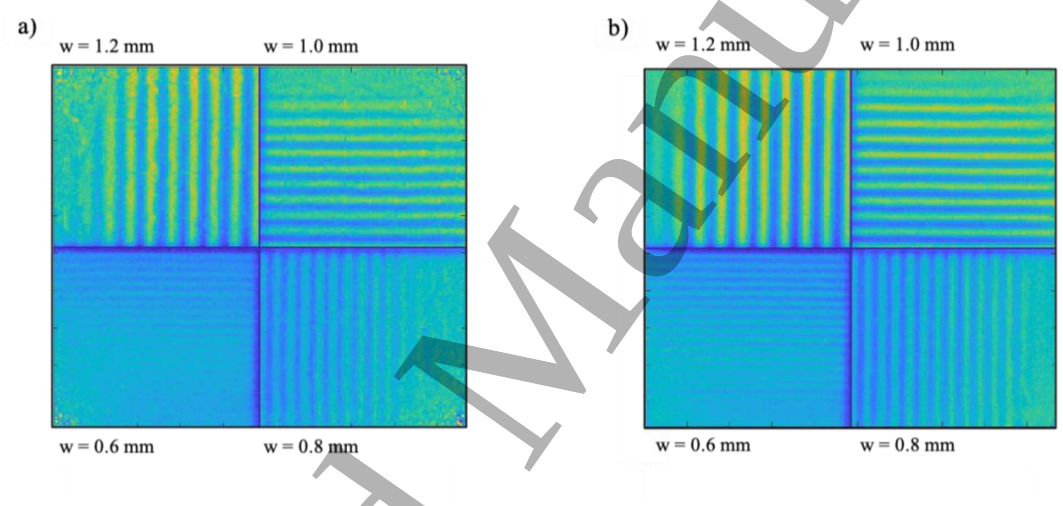

Figure 10 Bar phantom measurement with a) the MNN positioning and b) the neural network positioning.

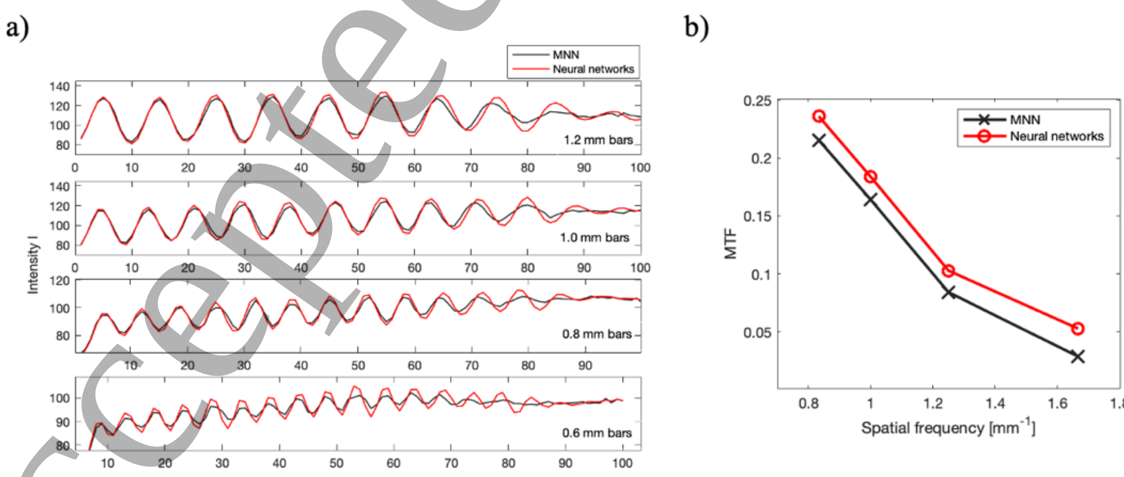

Figure 11 Evaluation of the bar phantom. a) The summed line profiles of the bar phantom. b) The modulation transfer function (MTF) of the detector.

In Figure 10 the bar patterns can be visually inspected from the MNN algorithm (left) and the neural network (right). The bar patterns can be well distinguished for all bar sizes with both algorithms. A more quantitative evaluation is shown in Figure 11. On the left the summed line profiles are presented. From these profiles the output modulation M_{out} is calculated. The MTF (Figure 11 b)) is calculated from M_{out} and the input modulation M_{in} which was obtained from simulations (0.94). It is given in line pairs per mm. The object contrast for the largest 1.2 mm bars (spatial frequency of 0.8 mm) is 22% and 24% for MNN and neural networks respectively. For the smallest bars of 0.6 mm (spatial frequency of 1.67 mm^{-1}) the object contrast is 2.9% and 5.3%.

3.6 2D resolution improvement by adding DOI layers

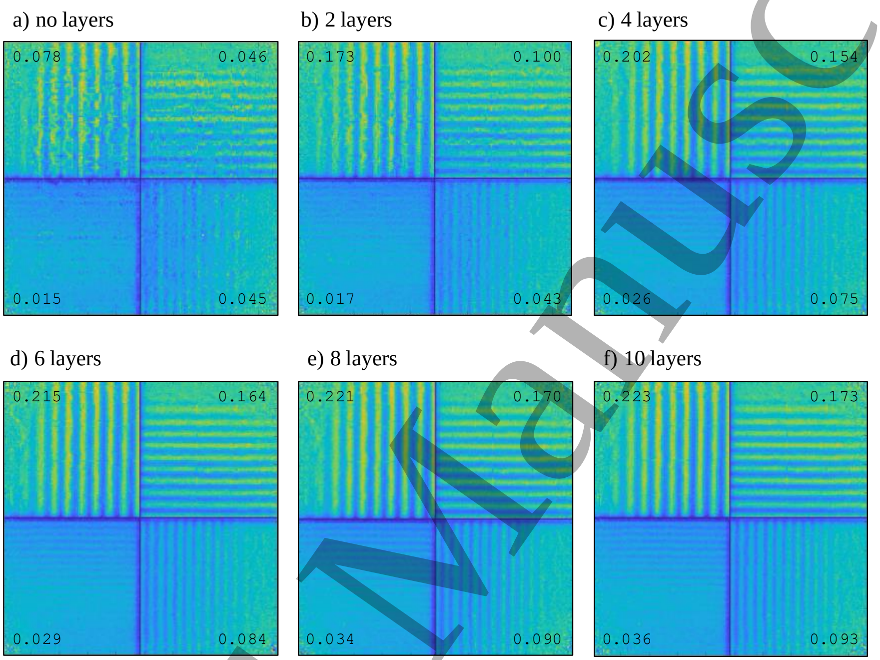

Figure 12 Bar phantom measurement with MNN positioning using up to 10 layers a) - f). MTF values are stated in the corner of each quadrant.

The 2D spatial resolution that is achieved with the MNN algorithm depends amongst other factors on the implementation of DOI layers. In Figure 12 the improvement can be seen between not using any DOI layers and a 10-layer DOI implementation. MTF values are stated in the corner of each quadrant. The most substantial improvement for this detector can be seen between layers 1 and 6. Here the MTF values for the largest bar size increase from 7.8% to 21.5% for the smallest bar size the MTF increases from 1.5% to 2.9%. Between 6 to 10 layers the improvement is limited. Here the MTF values for the largest bar size increase from 21.5% to 22.3% for the smallest bar size the MTF increases from 2.9% to 3.6%. For the neural network the 2D resolution does not depend on DOI layers.

4. Discussion

The mean spatial resolution obtained with neural networks is 1.14 mm FWHM for the whole detector and 1.02 mm in the centre excluding the edge region. Therefore, the novel neural network shows superior positioning performance to the MNN positioning algorithm by 2.6% and 9.7% respectively. The degradation towards the edges is typical for these detectors and is due to the scintillation light truncation. The measured PSFs at the edges are broader on the one hand but also not well characterized by Gaussian distributions that are used to calculate the FWHM. As can be seen in the uniformity measurement (Figure 8), events at the edges are often positioned at few very specific pixels leading to very good FWHM values. However, they are also connected to larger bias values. Hence, the fitting and resulting FWHM values at the very edges need to be taken with caution and median values or values excluding the edges are more reliable. In Figure 5 we see that the neural network shows a more uniform positioning performance especially at the edges compared to the MNN algorithm. The mean 2D bias is 0.59 mm for MNN and 0.2 mm for the neural network. In the centre the bias is 0.26 mm and 0.09 mm respectively. Note that this resolution is obtained with only 16 channels obtained from 6x6 mm^2 SiPMs that characterize the respective light spread functions (LSFs). Further improvements could be obtained by reading out more SiPM channels, that means 64 channels (8x8) when reading out each individual SiPM signal instead of one signal from each row and column (8+8). Another option that can further improve the results is using smaller SiPM pixels e.g., 3x3 mm^2 pixels in a 16x16 array reading out 32 or 256 channels. In previous simulation studies (Stockhoff *et al* 2019) we found that with an MNN approach for 6x6 mm^2 pixels (as used in this setup) a single channel readout does not significantly improve spatial resolution. The study also showed that a reduction of the SiPM pixel size to 3x3 mm^2 can improve the resolution by ~20% with summed channel readout and that a single channel readout with 256 channels further improves the resolution by another 7%. The next logical step would therefore be a reduction of the pixel size if better spatial resolution would be desired.

The experimental results do not include a correction to account for the resolution degradation introduced by the calibration beam diameter. The beam at its smallest diameter is here 0.6 mm. The collimator geometry leads to a spread of that beam with increasing distance to the collimator. The final beam width at the light extraction side of the crystal is slightly above 1 mm.

We tested calibrating the detector with a larger calibration beam diameter of 1 mm to estimate the effect the calibration beam has on the obtainable resolution. As mentioned above also the 1 mm collimated beam spreads with distance to the collimator. Results show that when the algorithms were trained with the data from the 1 mm beam and then tested on the 0.6 mm beam data, for the neural network, there is barely any degradation in terms of FWHM. The MNN algorithm just slightly degrades. We showed that the source diameter of 1 mm allows calibration at higher count rates while not causing much degradation on the detector performance. Note that the spatial resolution that we measure here depends strongly on the evaluation dataset. If we evaluated this detector with the data of the 1 mm collimator we would see a worse resolution and reversely the resolution would still improve significantly if ground truth data (without a beam diameter) would be available for testing (Stockhoff *et al* 2020). However, that does not change the actual performance that the detector will have on system level.

The main factors that could cause the performance differences between the two positioning algorithms are discussed in this section. The fraction of Compton scattered events is ~60% and has a large influence on the overall positioning performance (Decuyper *et al* 2021). The neural network is trained on many individual events while for the MNN database we use the mean of many signals which acts like a filter for PSFs of scattered events. The positioning of scattered events might therefore be improved with the neural networks. The output of the MNN algorithm is a discrete position depending on the degree of interpolation that is applied. The neural network on the contrary is able to provide continuous coordinates as an output. However, it is also prone to overfitting on the discrete calibration positions. Therefore, an additional dataset with signals of intermediate positions is needed to cross-check for overfitting in the training process. In terms of timing the neural network takes more time to be trained but once the training is finished positioning can be accomplished much faster. The MNN algorithm is comparing each event to the complete reference dataset which is computationally more intensive. This increases with higher degrees of interpolation and with the number of implemented DOI layers.

Besides very good intrinsic spatial resolution DOI estimation is an attractive feature of monolithic detectors. The variance of the LSF gives a direct measure of the DOI and can be easily extracted from the measured signal. However, with large monolithic crystals it is very difficult to quantify DOI performance. Obtaining depth dependent data from an experimental setup e.g., with an irradiation from the side has two main drawbacks. Firstly, the fact that most events will be captured at the very edge of the crystal and secondly, the Compton scatter direction is dependent on the incident angle of the gamma photon thus a side irradiation changes the measured light distributions for scattered events which are more than half of the events. Therefore, we compare the number of events in each depth-layer with (i) theoretically calculated numbers and (ii) simulated data, where the real DOI of the event is known. For MNN the overall DOI distribution is similar to what we expect but there is a large number of events in the sixth layer (close to readout array). This is related to the mispositioning of Compton scattered events when the actual photoelectric effect occurs deeper inside the crystal than the first interaction. This was previously shown in simulations. An implementation in neural networks with the variance as a measure of the depth shows that neural networks on the contrary are able to position scattered events more reliably. Ideally DOI studies should be linked to simulated data since this is the most accurate way to obtain ground truth data.

The measured energy resolution for the whole detector is 11.03%. The major degradations in the corner regions could be linked to the crystal, crystal finish or reflector. In separate experiments we turned the crystal while the rest of the setup stayed as it is. The degradation could still be linked to the specific corner of the scintillator. Experiments using other crystals showed also a degradation in the corners but with different emphasis. Thus, for more uniform and better energy resolution towards the corners the crystal and/or reflector quality should be examined.

The uniformity of the detector is clearly influenced by the underlying 8x8 SiPM pixel grid (Figure 8). When most optical photons are detected by a single SiPM pixel the algorithms are not able to position the event more accurately than in the centre of that pixel. In Figure 9 the origin of the artifacts becomes clearer by looking at the uniformity as a function of the estimated interaction depth of the photons. Especially towards the SiPM array in layer 5 and 6 uniformity starts to degrade. An improvement could be achieved by using smaller SiPMs or a light guide. Important to be aware of is that for the neural network a uniformity measurement is very useful to check for overfitting. During the training the overall positioning performance improves uniformly over the whole detector until the point that the performance at the discrete calibration positions keeps improving while the other positions start degrading. At that point the network is overfitting and detector performance will become non-uniform. In the uniformity histogram more events would be drawn towards the discrete 49x49 calibration grid forming a grid of hot spots. This effect is not observed here proving limited or no overfitting is present.

The bar phantom measurement gives a visual impression on the detector resolution over the complete field of view. The neural network can distinguish bars down to 0.6 mm with >5% contrast determined by the MTFs while the MNN algorithm is just below the 5% mark. The FWHM value is calculated as the smallest resolvable bar times 1.4 - 2 (Cherry *et al* 2012). Thus, the bar phantom measurement shows a detector resolution of 0.84 - 1.2 mm FWHM for neural networks and is in the range of what was evaluated with the PSFs. Note that for example in the bottom left quadrant the bars can be distinguished all the way to the left edge while they cannot be distinguished towards the bottom edge. This is due to the source position and angle of the gamma rays penetrating the bars. The impression of a central cone shape in contrast enhancement is a combination of these oblique incidence angles at the edges and a general worse detector capability to resolve events towards the edges. If a more perpendicular irradiation could be provided the resolution would improve more towards the edges as well.

Both algorithms show similar spatial resolution values (~0.1 mm difference). However, the artificial neural network provided more uniform performance over the full detector and smaller positioning bias. Furthermore, the DOI performance was improved with neural networks mainly due to improved positioning of scattered events. The bar phantom measurement provides additional support of the determined detector performance and spatial resolution at the detector centre, edges and corners. The detector resolution using neural networks is 1.13 mm FWHM over the whole detector and 1.02 mm FWHM without the edges. This is expectedly exceeding the resolution of PET detectors in the field that have a greater thickness than 16 mm (Borghi *et al* 2015, González-Montoro *et al* 2019, Bruyndonckx *et al* 2007). In (González-Montoro *et al* 2019) a remarkable detector spatial resolution of 0.9 mm FWHM is reported with a only slightly thinner crystal of 15 mm thickness. A notable difference is that the spatial resolution presented in our work is not corrected for the beam source diameter. In (González-Montoro *et al* 2019) a great effort is done to isolate the source size from the measured FWHM values leading to a better estimate of the intrinsic spatial resolution. Other detectors that have better spatial resolution are significantly thinner such as (Borghi *et al* 2015) with 1.1 mm spatial resolution at 10 mm thickness or (Mollet *et al* 2017) with 0.76 mm spatial resolution at 8 mm thickness.

5. Conclusion

In this work we presented a monolithic detector design aiming to serve high-resolution but lower cost clinical PET systems while maintaining high sensitivity. The targeted detector resolution of 1.3 mm intrinsic FWHM needed to reach a 2 mm resolution on system level (with bore diameter of 65 cm) was exceeded with a MNN algorithm and 1.13 mm FWHM, as well as with a neural network achieving 1.02 mm FWHM. The 6-layer DOI positioning will also result in a uniform system spatial resolution over the full FOV.

Acknowledgements

References

Alberts I, Hünermund J, Prenosil G, Mingels C, Bohn K P, Viscione M, Sari H, Vollnberg B, Shi K, Afshar-oromieh A and Rominger A 2021 Clinical performance of long axial field of view PET / CT : a head-to-head intra-individual comparison of the Biograph Vision Quadra with the Biograph Vision PET / CT *Eur. J. Nucl. Med. Mol. Imaging*

Alva-Sánchez H, Zepeda-Barrios A, Díaz-Martínez V D, Murrieta-Rodríguez T, Martínez-Dávalos A and Rodríguez-Villafuerte M 2018 Understanding the intrinsic radioactivity energy spectrum from 176Lu in LYSO/LSO scintillation crystals *Sci. Rep.* **8** 1–7

Borghi G, Peet B J, Tabacchini V and Schaart D R 2016a A 32 mm x 32 mm x 22 mm monolithic LYSO:Ce detector with dual-sided digital photon counter readout for ultrahigh-performance TOF-PET and TOF-PET/MRI *Phys. Med. Biol.* **61** 4929–49

Borghi G, Tabacchini V and Schaart D R 2016b Towards monolithic scintillator based TOF-PET systems: practical methods for detector calibration and operation *Phys. Med. Biol.* **61** 4904–28

Borghi G, Tabacchini V, Seifert S and Schaart D R 2015 Experimental validation of an efficient fan-beam calibration procedure for k-nearest neighbor position estimation in monolithic scintillator detectors *IEEE Trans. Nucl. Sci.* **62** 57–67

Bruyndonckx P, Lemaître C, Schaart D, Maas M, van der Laan D J (jan., Krieguer M, Devroede O and Tavernier S 2007 Towards a continuous crystal APD-based PET detector design *Nucl. Instruments Methods Phys. Res. Sect. A Accel. Spectrometers, Detect. Assoc. Equip.* **571** 182–6

Bruyndonckx P, Léonard S, Tavernier S, Lemaître C, Devroede O, Wu Y and Krieguer M 2004 Neural network-based position estimators for PET detectors using monolithic LSO blocks *IEEE Trans. Nucl. Sci.* **51** 2520–5

Cherry S R, Sorenson J A and Phelps M E 2012 *Physics in Nuclear Medicine* (Elsevier Saunders)

Chinn G, Olcott P D and Levin C S 2013 Sparse signal recovery methods for multiplexing PET detector readout *IEEE Trans. Med. Imaging* **32** 932–42

van Dam H T, Seifert S, Vinke R, Dendooven P, Löhner H, Beekman F J and Schaart D R 2011 Improved nearest neighbor methods for gamma photon interaction position determination in monolithic scintillator PET detectors *IEEE Trans. Nucl. Sci.* **58** 2139–47

Decuyper M, Stockhoff M, Vandenberghe S and Van Holen R 2021 Artificial neural networks for positioning of gamma interactions in monolithic PET detectors *Phys. Med. Biol.* **66** 075001

Deprez K, Van Holen R, Vandenberghe S and Staelens S 2011 Design of a high resolution scintillator based SPECT detector (SPECTatress) *Nucl. Instruments Methods Phys. Res. Sect. A Accel. Spectrometers, Detect. Assoc. Equip.* **648** S107–10

España S, Deprez K, Van Holen R and Vandenberghe S 2013 Fast calibration of SPECT monolithic scintillation detectors using un-collimated sources *Phys. Med. Biol.* **58** 4807–25

España S, Marcinkowski R, Keereman V, Vandenberghe S and Van Holen R 2014 DigiPET: Sub-millimeter spatial resolution small-animal PET imaging using thin monolithic scintillators *Phys. Med. Biol.* **59** 3405–20

Freire M, Gonzalez-Montoro A, Sanchez F, Benlloch J M and Gonzalez A J 2019 Calibration of Gamma Ray Impacts in Monolithic-Based Detectors Using Voronoi Diagrams *IEEE Trans. Radiat. Plasma Med. Sci.* **4** 350–60

Gonzalez-Montoro A, Gonzalez A J, Pourashraf S, Miyaoka R S, Bruyndonckx P, Chinn G, Pierce L A and Levin C S 2021 Evolution of PET Detectors and Event Positioning Algorithms Using Monolithic Scintillation Crystals *IEEE Trans. Radiat. Plasma Med. Sci.* **5** 282–305

González-Montoro A, Sánchez F, Bruyndonckx P, Cañizares G, Benlloch J M and González A J 2019 Novel method to measure the intrinsic spatial resolution in PET detectors based on monolithic crystals *Nucl. Instruments Methods Phys. Res. Sect. A Accel. Spectrometers, Detect. Assoc. Equip.* **920** 58–67

González-Montoro A, Sánchez F, Martí R, Hernández L, Aguilar A, Barberá J, Catret J V., Cañizares G, Conde P, Lamprou E, Martos F, Sánchez S, Vidal L F, Benlloch J M and González A J 2018 Detector block performance based on a monolithic LYSO crystal using a novel signal multiplexing method *Nucl. Instruments Methods Phys. Res. Sect. A Accel. Spectrometers, Detect. Assoc. Equip.* **912** 372–7

Gundacker S, Acerbi F, Auffray E, Ferri A, Gola A, Nemallapudi M V, Paternoster G, Piemonte C and Lecoq P 2016 State of the art timing in TOF-PET detectors with LuAG, GAGG and L(Y)SO scintillators of various sizes coupled to FBK-SiPMs *J. Instrum.* **11** P08008–P08008

Hu P, Zhang Y, Yu H, Chen S, Tan H, Qi C, Dong Y, Wang Y, Deng Z and Shi H 2021 Total-body 18F-FDG PET/CT scan in oncology patients: how fast could it be? *Eur. J. Nucl. Med. Mol. Imaging*

Iborra A, González A J, González-Montoro A, Bousse A and Visvikis D 2019 Ensemble of neural networks for 3D position estimation in monolithic PET detectors *Phys. Med. Biol.* **64** 20pp

Ito M, Hong S J and Lee J S 2011 Positron emission tomography (PET) detectors with depth-of- interaction (DOI) capability *Biomed. Eng. Lett.* **1** 70–81

Karp J S, Viswanath V, Geagan M J, Muehllehner G, Pantel A R, Parma M J, Perkins A E, Schmall J P, Werner M E and Daube-Witherspoon M E 2020 PennPET explorer: Design and preliminary performance of a whole-body imager *J. Nucl. Med.* **61** 136–43

Krishnamoorthy S, Blankemeyer E, Mollet P, Surti S, Van Holen R and Karp J S 2018 Performance evaluation of the MOLECUBES β -CUBE—a high spatial resolution and high sensitivity small animal PET scanner utilizing monolithic LYSO scintillation detectors *Phys. Med. Biol.* **63** 1–12

Lamprou E, Gonzalez A J, Sanchez F and Benlloch J M 2020 Exploring TOF capabilities of PET detector blocks based on large monolithic crystals and analog SiPMs *Phys. Medica* **70** 10–8

Lecoq P, Morel C, Prior J O, Visvikis D, Gundacker S, Auffray E, Križan P, Turtos R M, Thers D, Charbon E, Varela J, De La Taille C, Rivetti A, Breton D, Pratte J F, Nuyts J, Surti S, Vandenberghe S, Marsden P, Parodi K, Benlloch J M and Benoit M 2020 Roadmap toward the 10 ps time-of-flight PET challenge *Phys. Med. Biol.* **65**

Levin C S and Hoffman E J 2000 Erratum: Calculation of positron range and its effect on the fundamental limit of positron emission tomography system spatial resolution (Physics in Medicine and Biology (1999) 44 (781-799)) *Phys. Med. Biol.* **45** 559

Ling T, Lewellen T K and Miyaoka R S 2007 Depth of interaction decoding of a continuous crystal detector module *Phys. Med. Biol.* **52** 2213–28

Marcinkowski R, Mollet P, Van Holen R and Vandenberghe S 2016 Sub-millimetre DOI detector based on monolithic LYSO and digital SiPM for a dedicated small-animal PET system *Phys. Med. Biol.* **61** 2196–212

Miyaoka R S, Ling T, Lockhart C and Lewellen T K 2010 Calibration procedure for a continuous miniature crystal element (cMiCE) detector *IEEE Trans. Nucl. Sci.* **57** 1023–8

Mollet P, Deprez K, Vandeghinste B, Neyt S, Marcinkowski R, Vandenberghe S and Van Holen R 2017 The β-CUBE, a high-end compact preclinical benchtop PET for total body imaging *J. Nucl. Med.* **58** 393

Müller F, Schug D, Hallen P, Grahe J and Schulz V 2018 Gradient Tree Boosting-based Positioning Method for Monolithic Scintillator Crystals in Positron Emission Tomography *IEEE Trans. Radiat. Plasma Med. Sci.* **2** 411–21

Pan T, Einstein S A, Kappadath S C, Grogg K S, Lois Gomez C, Alessio A M, Hunter W C, El Fakhri G, Kinahan P E and Mawlawi O R 2019 Performance evaluation of the 5-Ring GE Discovery MI PET/CT system using the national electrical manufacturers association NU 2-2012 Standard *Med. Phys.* **46** 3025–33

Pierce L A, Hunter W C J, Haynor D R, MacDonald L R, Kinahan P E and Miyaoka R S 2014 Multiplexing strategies for monolithic crystal PET detector modules *Phys. Med. Biol.* **59** 5347–60

Pierce L A, Pedemonte S, Dewitt D, Macdonald L, Hunter W C J, Van Leemput K and Miyaoka R 2018 Characterization of highly multiplexed monolithic PET / gamma camera detector modules *Phys. Med. Biol.* **63** 16pp

Rausch I, Ruiz A, Valverde-Pascual I, Cal-González J, Beyer T and Carrio I 2019 Performance evaluation of the VereoS PET/CT system according to the NEMA NU2-2012 standard *J. Nucl. Med.* **60** 561–7

van Sluis J, de Jong J, Schaar J, Noordzij W, van Snick P, Dierckx R, Borra R, Willemsen A and Boellaard R 2019 Performance Characteristics of the Digital Biograph Vision PET/CT System *J. Nucl. Med.* **60** 1031–6

Spencer B A, Berg E, Schmall J P, Omidvari N, Leung E K, Abdelhafez Y G, Tang S, Deng Z, Dong Y, Lv Y, Bao J, Liu W, Li H, Jones T, Badawi R D and Cherry S R 2020 Performance evaluation of the uEXPLORER Total-body PET/CT scanner based on NEMA NU 2-2018 with additional tests to characterize long axial field-of-view PET scanners *J. Nucl. Med.* jnumed.120.250597

Stockhoff M, Van Holen R and Vandenberghe S 2020 Identifying potential sources of resolution degradation in monolithic scintillators: simulations vs experiments *IEEE MIC Poster 2020*

Stockhoff M, Van Holen R and Vandenberghe S 2019 Optical simulation study on the spatial resolution of a thick monolithic PET detector *Phys Med Biol* **64** 13pp

Surti S, Pantel A R and Karp J S 2020 Total Body PET: Why, How, What for? *IEEE Trans. Radiat. Plasma Med. Sci.* **4** 283–92

Thoen H, Keereman V, Mollet P, Van Holen R and Vandenberghe S 2013 Influence of detector pixel size, TOF resolution and DOI on image quality in MR-compatible whole-body PET *Phys. Med. Biol.* **58** 6459–79

Vandenberghe S, Mikhaylova E, Brans B, van Holen R, Schaart D R and Karp J S 2017 PET 20.0: A cost efficient, 2.00 mm resolution total body monolithic PET with very high sensitivity and an adaptive axial FOV up to 2.00 m *Annual Congress of the European Association of Nuclear Medicine* (Vienna) p 305

Vandenberghe S, Moskal P and Karp J S 2020 State of the art in total body PET *EJNMMI Phys.* **7** 35

Wang Y, Zhu W, Cheng X and Li D 2013 3D position estimation using an artificial neural network for a continuous scintillator PET detector. *Phys. Med. Biol.* **58** 1375–90

Yang Q, Kuang Z, Sang Z, Yang Y and Du J 2019 Performance comparison of two signal multiplexing readouts for SiPM-based pet detector *Phys. Med. Biol.* **64**